Analytical model for metal–insulator–metal mesh waveguide architectures

Charles Lin,[1,*] Mohamed A. Swillam,[2] and Amr S. Helmy[1]

[1]*Department of Electrical and Computer Engineering, University of Toronto, Toronto M5S 3G4, Canada*
[2]*Department of Physics, School of Science and Engineering, The American University in Cairo, New Cairo 11835, Egypt*
**Corresponding author: charleschihchin.lin@utoronto.ca*

Received May 29, 2012; revised September 4, 2012; accepted September 5, 2012;
posted September 12, 2012 (Doc. ID 168989); published October 29, 2012

Metal–insulator–metal (MIM) waveguide mesh structures utilize X-junctions as power distribution elements to create interference and feedback effects, thereby providing rich device functionality. We present a generalized analytical model for MIM mesh structures by incorporating a modified characteristic impedance model for MIM junctions into the scattering matrix formalism. The modified impedance model accounts for metal absorption and provides accurate prediction of plasmonic field distribution at X-junctions in terms of both magnitude and phase. Closed-form expressions for 2×1 and 2×2 MIM mesh architectures as well as MIM stub structures are then obtained and are dependent only on waveguide geometry and junction configuration. The model does not require numerically extracted parameters, and results agree, within a few percent, with those obtained from finite-difference time-domain method for both two-dimensional and three-dimensional waveguide geometries. The capability of the model for efficient design and optimization of junction-based MIM devices is demonstrated through the development of various filter and resonant devices.

OCIS codes: 000.4430, 350.4238, 250.5403, 240.6680, 240.6690, 050.6624.

1. INTRODUCTION

Guided waves that utilize surface plasmon polaritons (SPPs) possess properties that can empower numerous applications with their ability to guide light at the subwavelength scale. The strong field enhancement near the metal–dielectric surfaces of SPP waveguides has been exploited for sensing and surface-enhanced Raman scattering [1,2] applications. With sub-100 nm modal confinement, SPP waveguides are also a promising platform for high bandwidth optical interconnects that bridge the scale mismatch between microscale dielectric optical devices and nanoscale electronics [3]. These subwavelength waveguides are compatible with conventional complementary metal–oxide–semiconductor processes, making them an ideal candidate for optical interconnect at the transistor level of the integrated circuit stacks.

Of the various configurations of SPP waveguides, the metal–insulator–metal (MIM) waveguide is suitable for both optical interconnect and sensing applications. It usually consists of a subwavelength dielectric core surrounded by metallic slabs in the horizontal direction [Fig. 1(a)]. The continuity of the transverse electric field parallel to the metal–dielectric interface prevents charge accumulation, and thus the waveguide only supports transverse magnetic (TM) mode in the visible and near-IR regimes [4]. For core width smaller than a few hundred nanometers, the effective index of the waveguide has weak wavelength dependence and is controlled primarily by the core width; thus, a narrower core would result in a higher effective index due to the enhanced interaction between SPP fields and metal claddings. Since the mode is confined in the dielectric region, where it penetrates only the skin depth (~25 nm) of the adjacent metal regions [4], the transverse modal dimension is controlled by the width of the dielectric core and can be reduced to few tens of nanometers [5], allowing dense integration of plasmonic interconnects. With the majority of the optical power residing within the core, the waveguide is also highly sensitive to local environmental index change. When extended into the 3D configuration, where the MIM waveguide is embedded in dielectric in the vertical dimension [Fig. 1(b)], the slot can serve as a microfluidic channel that enables targeted delivery of analytes for both surface and bulk biosensing [6]. Furthermore, recent experimental realization of a highly efficient coupling mechanism between MIM waveguide and conventional silicon waveguide has been demonstrated [7]. This nanoscale, nonresonant, and wideband coupling scheme opens the door for a wide range of silicon-plasmonic hybrid applications.

The tradeoff associated with utilizing the nanoscale confinement of MIM waveguides, however, is the significant metal absorption loss. With a sub-100 nm core, the waveguide propagation loss is a few decibels per micrometer, and the propagation length (distance in which the intensity of the transverse field drops to $1/e$) is less than 10 μm [8]. Thus, a crucial criterion for designing high performance MIM devices is that the footprint can only be on the scale of a few micrometers.

Numerous optical components based on MIM waveguides have been proposed, such as splitters [9], interferometers [10], switches [11], and demultiplexer [12]. The design of these resonance-based devices is based on the coupling between nonintersecting MIM cavities. In order for the tunneling of the electromagnetic field to take place, the separation between cavities needs to be less than the metal skin depth, which requires stringent fabrication control. In addition, these designs are often several micrometers in size, because the device subcomponents are cascaded in a sequential fashion.

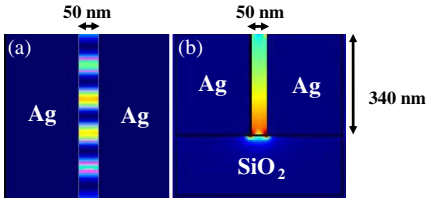

Fig. 1. (Color online) (a) Top view and (b) cross-sectional view of the total electric field intensity of the propagating MIM fundamental mode at $\lambda = 1550$ nm. The waveguide is 340 nm tall with a 50 nm core.

Recently, another class of MIM devices has emerged and is based on networks of intersecting MIM waveguide junctions. It was reported that, for waveguides with subwavelength core width, the MIM mode can efficiently propagate over sharp bends and optical power can be evenly distributed among the arms of an orthogonally intersected waveguide junction [13,14]. Treating MIM junctions as compact power distribution elements, nanoscale splitters [13] and demultiplexers [15] have already been proposed. By using these junctions as the building blocks for larger two-dimensional (2D) mesh structures, the simultaneous power distribution at various junctions leads to complex interference patterns. This optical interference can then be utilized to create resonance and/or feedback effects within the mesh structure, providing rich functionalities at the device level. For example, the resonance effect in a plasmonic 2×2 mesh structure consisting of four X-junctions has already been investigated and exploited for color routers [16]. Furthermore, we have recently demonstrated an MIM filter that uses the feedback effect in T-junctions to attain various categories of filter responses ranging from wideband flat transmission to narrowband notch effect [17]. Previous investigation shows that a 10% change in the waveguide width results in a 3% shift of the resonance wavelength of a 1 μm radius dielectric ring resonator, but only 0.3% in the case of an MIM feedback structure with a footprint that is two orders of magnitude smaller [18]. This is because subwavelength MIM junctions have a weaker wavelength dependence due to the significant metal absorption loss. Therefore, these nanoscale mesh structures are much more tolerant of process variations even though their Q-factor is several orders of magnitude smaller compared to that of their dielectric counterparts.

Despite the promise that these mesh structures hold for nanophotonic circuits, the design of MIM junction-based devices is at the moment hindered by the lack of suitable analytical models. The aforementioned junction-based devices are primarily modeled using the finite-difference time-domain (FDTD) technique, which is computationally intensive, has a significant memory requirement, and does not provide upfront physical insights into device characteristics. Moreover, relying on a numerical method to perform device sensitivity analysis and optimization processes is inefficient especially for larger and more complex mesh structures. Because MIM waveguides have nanoscale field confinement, the required simulation mesh size can only be a few nanometers. This means that the required computational resources will scale drastically with the dimensions and complexity of the network. To reduce the computational cost, the scattering matrix (S-matrix) method commonly used for microwave circuit design has been proposed to analyze the interactions between different parts of a MIM network structure [16]. Although closed-form transmission expression for the overall structure can be derived from the S-matrix, modeling individual junctions is still based on a precompiled library of numerically extracted waveguide dispersion characteristics and junction power distribution ratios. In order to achieve realistic design and optimization cycle durations for functional devices using MIM mesh structures, there is still a need for an analytical model that can handle arbitrary combination of junctions without requiring FDTD-extracted parameters.

For the modeling of MIM junctions, a waveguide characteristic impedance model has been proposed with good agreement compared to its numerical counterpart [13,17,19]. Unlike dielectric waveguides or other SPP waveguide configurations, MIM waveguides have uniform transverse field confinement similar to that of a perfect electric conductor (PEC) parallel-plate waveguide. Therefore, characteristic impedance can be uniquely defined, and transmission line analysis is applicable for analyzing MIM junctions. Providing a basic description of the junction behavior, this impedance model can then be readily incorporated into the S-matrix formulation to analyze a network of cascaded MIM junctions. Studies up until now, however, have focused on utilizing the impedance model for MIM bends, T-junctions [13,19], stub structures [20], and waveguide discontinuities [21]. Investigation on the suitability of the impedance model for X-junctions with asymmetric arm widths, the most generalized junction configuration, is still absent. Furthermore, loss and phase information in MIM waveguide junctions are also not accounted for. They are critical when the junctions are cascaded into network structures with strong internal interference effect. Finally, as the widths of the junction arms and the operating wavelength are varied, the dielectric discontinuity at the center of the X-junction can cause the breakdown of the equal four-way splitting behavior, potentially affecting the applicability of the impedance model. The impedance model's region of validity for designing subwavelength devices has not yet been defined.

In this paper, a generic analytical model for MIM mesh structures is presented. We incorporate the impedance model into the S-matrix formalism and for the first time generalize this methodology to 2D MIM mesh structures. We first show that the impedance model can be extended to provide both the amplitude and phase information for symmetric as well as asymmetric X-junctions. Then, we demonstrate that by adopting the S-matrix formulation to model the interaction between various junctions, it is possible to parameterize a plasmonic mesh structure and derive a closed-form transmission expression that is dependent only on the mesh topology. This methodology enables the design and optimization of 2D MIM mesh structures without FDTD-extracted parameters. The validity and versatility of our model are then examined by first comparing the analytical and numerical results for 2×1 and 2×2 networks made out of MIM waveguides with uniform core width and then extending this approach to generic 2D architectures such as stub-loaded mesh and resonance-enhanced network structures with varying core width. The capability of this design scheme is further elucidated through discussions on the model's scalability for accommodating larger and 3D network configurations as well as the ability to provide device sensitivity analysis.

2. ADAPTATION OF IMPEDANCE MODEL TO MIM *X*-JUNCTIONS

To develop an analytical model that does not rely on FDTD-extract parameters, the junction impedance model first needs to be extended to include waveguide absorption loss and predict both the amplitude and phase of the resulting plasmonic wave in each junction arm. The fundamental unit of MIM mesh structures is the *X*-junction, which consists of two orthogonally intersecting MIM waveguides (Fig. 2). When the *X*-junction is excited from one arm, the optical power is distributed among the four junction arms as represented by reflection and transmission coefficients r and t_i. The dielectric discontinuity at the center of the junction can excite higher order evanescent modes, which will then decay exponentially in the single-mode junction arms. Thus, given that the metal cladding is thicker than the metal skin depth, each junction arm can be treated as a discrete single-mode waveguide that does not couple to the others except at the center of the junction. For MIM waveguides with dielectric cores that are much smaller compared to the operating wavelength ($d/\lambda_o \sim 0$), it has been reported that quasistatic approximation can be applied and the waveguides can be treated as PEC parallel-plate waveguides [13]. Under quasistatic approximation, an MIM *X*-junction is equivalent to a set of discrete transmission lines, where each junction arm is represented by its own characteristic impedance ($Z = V/I$). Since the electromagnetic fields of MIM waveguides are confined primarily in the dielectric region, the approximations $V = \omega E_{\text{transverse}}$ and $I \alpha H_{\text{transverse}}$ can be applied to uniquely calculate the waveguide characteristic impedance. For MIM waveguides with a low index filling and core width of less than 200 nm, the impedance can be approximated to be [13,19]

$$Z_i(\omega, d_i) \approx \frac{\beta_{\text{MIM}}(\omega, d_i) d_i}{n^2 \omega \varepsilon_o}, \tag{1}$$

where β_{MIM} is the real part of the MIM propagation constant, d_i is the width of the junction arm, and n is the refractive index of the core dielectric medium. The waveguide impedance is primarily determined by the core width, since the propagation constant is also dependent on the width of the waveguide.

To calculate the power distribution at an *X*-junction, the input junction arm is represented as a transmission line with impedance Z_O, whereas the remaining junction arms are represented as transmission lines connected in series with total load impedance of Z_L. The reflection ($\hat{r}$) and transmission ($\hat{t}_i$) coefficients for lossless *X*-junctions are defined to be

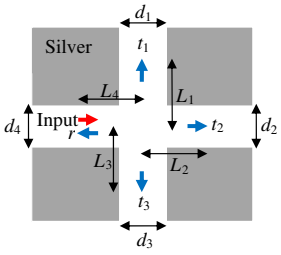

Fig. 2. (Color online) Schematic and parameters of an MIM *X*-junction.

$$\hat{r} = \left| \frac{Z_L - Z_O}{Z_L + Z_O} \right| \quad \text{and} \quad \hat{t}_i = \left| \frac{2\sqrt{Z_o Z_L}}{Z_o + Z_L} P_i \right| = \left| \frac{2\sqrt{Z_o Z_L}}{Z_o + Z_L} \sqrt{\frac{Z_i}{Z_L}} \right|, \tag{2}$$

where Z_i is the impedance of output waveguide i, and the P_i factor distributes the transmitted light among the output waveguides according to their relative impedance. If the widths of the junction arms are not identical, then an individual set of reflection and transmission coefficients needs to be defined for the junction excitation from each direction.

Under quasistatic approximation, the excitation of an *X*-junction is analogous to placing a point source at the center of the junction, and thus the propagation distance of the plasmonic wave in each arm can be treated as identical [14]. As such, the reflection and transmission coefficients can simply be redefined as

$$\begin{aligned} r &= \hat{r} \exp(-(\alpha_4 + j\beta_4)(2L_4)), \\ t_i &= \hat{t}_i \exp(-[(\alpha_i + j\beta_i)(L_i) + (\alpha_4 + j\beta_4)(L_4)]), \end{aligned} \tag{3}$$

where α_i is the the total loss factor, β_i is the real part of the propagation constant for each junction arm, and L_i is the arm length.

To verify the validity of the modified impedance model, it is applied to both symmetric and asymmetric *X*-junctions and compared with numerical studies from FDTD simulations using commercial Lumerical software. The FDTD simulations are performed with a mesh size of 2.5 nm near the waveguide core and 5 nm in the rest of the computational domain. The perfectly matched layer absorbing boundary condition is used to terminate the simulation region. The Ag material model used is based on a higher order polynomial fitting of experimental data from Palik [22]. The source and power monitors are placed 200 and 400 nm away from the junction center, respectively, to allow higher order modes to diminish. Moreover, the loss factor α_i is assumed to be only the MIM waveguide propagation loss.

A symmetric *X*-junction 400 nm long arms and 100 wide nm air-filled core is first investigated. Since $Z_L = 3Z_o$, the impedance model predicts that the plasmonic wave will split evenly among the four junction arms. This is observed in FDTD simulations as shown from Fig. 3(a) to 3(d), where the optical intensities in all four arms are nearly identical over a large bandwidth. At wavelengths above 0.8 μm, the difference is less than 1%. This slight discrepancy is a result of scattering and higher order mode excitation at the center of the junction, which is negligible as long as the width of the core is in the subwavelength regime. On the other hand, as the operating wavelength is reduced, the modal intensity shifts toward the center of the core region, thereby transforming from a surface mode into a total-internal-reflection (TIR) mode. In this case, the MIM waveguide behaves like a dielectric waveguide and the amount of coupling into normal arms is significantly reduced. Despite the slight deviation at a lower wavelength, the shape of the spectral response is accurately modelled. In the interest of designing optical devices working in the telecommunication wavelength regime, the modified impedance model can provide accurate means for analyzing MIM

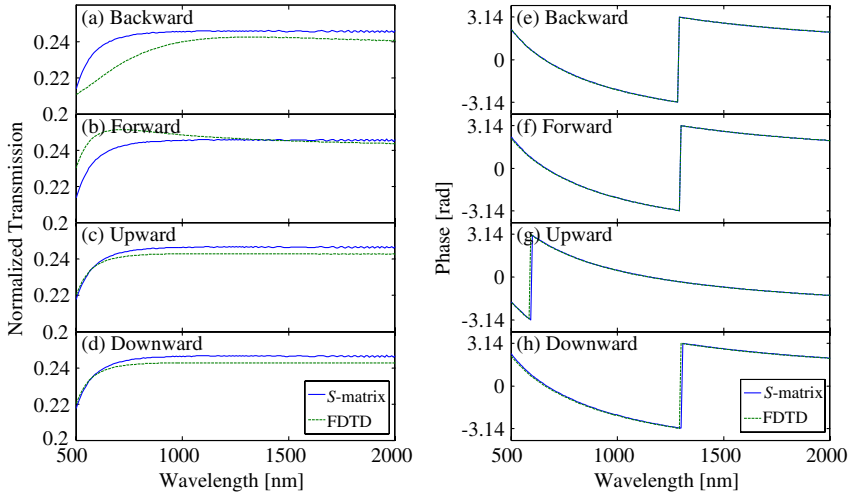

Fig. 3. (Color online) Comparison between FDTD and *S*-matrix modeling results of a symmetric *X*-junction with 100 nm cores and 400 nm arms. The junction is excited from the left horizontal arm, and both the normalized transmission and phase of the plasmonic waves in each junction arm are plotted.

waveguide junctions without any numerically extracted parameters.

The junction phase calculated using our model also demonstrates good agreement with FDTD simulations, as shown from Fig. 3(e) to 3(h). The phase in each arm is continuous across the spectrum and the discontinuities observed in the plot are not actually physical. Instead, they are the result of wrapping the phase information between the $-\pi$ to π range. The agreement further validates the applicability of the modified impedance model and indicates that under quasistatic approximation, the dielectric discontinuity at the center of the junction does not induce phase change and the plasmonic waves in all arms can also be assumed to have propagated over equal distances. In other words, phase accumulation is only attributed to propagation along the junction arms. Although the symmetric junction exhibits equal power distribution, the plasmonic wave in the upper arm has a π phase shift compared to that of other arms. This phenomenon is observed independent of waveguide configurations or the locations of the source and monitors in FDTD simulations.

The modified impedance model is also verified for an asymmetric *X*-junction where $d_1 = d_3 = 100$ nm and $d_2 = d_4 = 50$ nm (Fig. 4). Similar to the case of the symmetric *X*-junction, the discrepancy is less than 1% in the wavelength regime above 0.8 μm. Thus, with a subwavelength waveguide core, the asymmetry in *X*-junction arms does not affect the performance of the modified impedance model. In other words, the modified impedance model is confirmed to be applicable for modelling both intensity and phase of generalized *X*-junctions and can be incorporated into the *S*-matrix formulation.

Although the modified impedance model enables efficient design of junction-based MIM optical devices, the width of the waveguide core should be kept to less than a few hundred nanometers. Figure 5 shows the breakdown of perfect four-way splitting behavior in a symmetric *X*-junction as the core width is varied. The result displayed is normalized to remove the contribution of propagation loss in junction arms. The percent deviation is plotted for only one of the sideways arms, and it is identical for the other sideways arm. It can be observed that an MIM *X*-junction only exhibits perfect four-way splitting when the core width is approximately 120 nm. As the core width increases, the modal intensity shifts from the metal–dielectric interface toward the center of the slot, and the energy from the transverse component of the electric field is transferred into the longitudinal component. In this case, quasistatic approximation no longer holds and the characteristic impedance model breaks down. Behaving like a dielectric waveguide, most of the light would continue to propagate forward when reaching the junction. Since operating at a lower wavelength is analogous to increasing the width of the waveguide core, the percent deviation from equal splitting also increases as wavelength is decreased (Fig. 5).

With a sub-120 nm core width, the perfect equal splitting behavior of an *X*-junction also breaks down. As the width of the waveguide core decreases, the SPP waves become even more tightly confined to the metal–dielectric interfaces. Therefore, due to the continuity of the metal–dielectric interfaces, the MIM mode will preferentially divide among the sideways and backward junction arms. With a sub-120 nm waveguide core, quasistatic approximation still holds, but the assumption that the dielectric discontinuity at the center of the junction induces negligible loss and phase change is no longer valid. From Fig. 5, it can be observed that the normalized optical power in all of the arms is less than 25%, indicating the existence of additional loss mechanisms, such as metal absorption, scattering, and the excitation of single surface SPP modes and higher order MIM modes. Furthermore, since the amount of power in different junction arms are not identical, the assumption that the plasmonic wave in each arm has propagated over an equal distance is not valid over the entire spectrum. In order for the above assumptions to be valid and the model to provide analysis of MIM junctions with ±2% discrepancy in comparison to FDTD results, the core width needs to be less than 200 nm and the MIM mesh device should operate in the near-IR regime. Within the framework of designing compact optical sensors, circuitry, and interconnects near 1550 nm, these constraints are already satisfied.

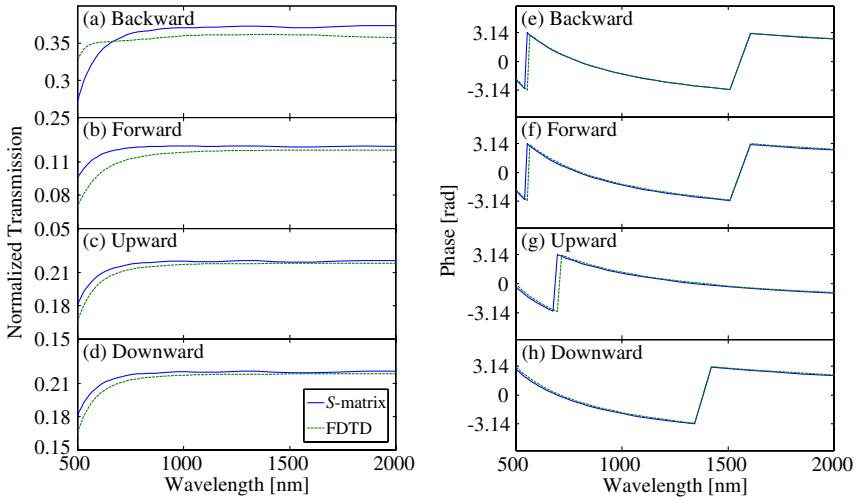

Fig. 4. (Color online) Comparison between FDTD and *S*-matrix modeling results of an asymmetric *X*-junction with 50 nm horizontal cores, 100 nm vertical cores, and 400 nm arms. The junction is excited from the left horizontal arm, and both the transmission and phase of the plasmonic waves in each junction arm are plotted.

Thus, the modified characteristic impedance model does not impose additional constraints on junction-based optical device design.

In our modified impedance model, the approximated formulation of waveguide characteristic impedance is used, and this is sufficient for modeling MIM mesh structures with sub-200 nm cores. The exact impedance formulation would provide a more accurate description of the waveguide impedance, especially for MIM waveguides with thicker dielectric cores (>200 nm) or high index filling [19]. Nonetheless, the dielectric-like modal profile of wider MIM waveguides would lead to the breakdown of equal four-way splitting behavior and using the exact impedance formulation would not significantly improve the model's performance.

On the other hand, the improvement provided by the exact formulation is also determined to be minimal in the sub-200 nm regime. This is because the exact and approximated impedance formulations match well when the SPP waves are strongly coupled [23]. To examine the effect of using the approximated formulation, the discrepancies between numerical and analytical results for symmetric and asymmetric *X*-junctions are compared (Figs. 3 and 4). The model's performance should degrade in the case of the asymmetric junction, since the approximated impedance formulation should introduce a slight error when calculating the relative impedance between junction arms. Nonetheless, the discrepancy is around 1% for both symmetric and asymmetric junctions. This suggests that although using the approximated impedance model does introduce errors, the discrepancies between numerical and analytical results are dominated by the additional loss mechanisms of the MIM waveguides. Therefore, within the region of validity of our modified impedance model, the approximated impedance formulation already provides sufficient accuracy for analyzing MIM mesh structures.

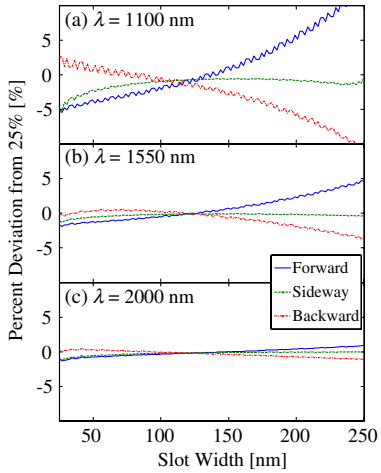

Fig. 5. (Color online) Model limitation demonstrated by the percent deviation from equal power splitting (25%) in a symmetric *X*-junction at (a) $\lambda = 1100$ nm, (b) $\lambda = 1550$ nm, and (c) $\lambda = 2000$ nm.

Although the exact impedance formulation does not offer significant improvement in accuracy for modeling generalized *X*-junctions, it may be appropriate for other junction geometries. For mesh structures that are made out of bends, *T*-junctions, and/or waveguide discontinuities, the coupling between orthogonal arms is more efficient and the equal four-way splitting behavior is preserved over a larger spectrum. Thus, the region of validity of the modified impedance model may be extended for specific mesh configurations.

3. SCATTERING MATRIX MODEL OF MIM MESH STRUCTURES

In order to model the interaction between *X*-junctions in an MIM mesh structure, the junction impedance model needs to be incorporated into the *S*-matrix formulation. The *S*-matrix method breaks down a network of structures into subcomponents, and the matrix elements relate the electric fields entering and exiting the various subcomponents. Since the mesh structure can be treated as a network of interconnected junctions, the *S*-matrix method is a suitable mathematical framework for analyzing the distribution of electromagnetic energy within the mesh as well as the resulting transmission responses at different output ports. The matrix elements are complex, since both the magnitude and phase of the electromagnetic waves are modified by the network topology.

By solving the *S*-matrix, a closed-form analytical expression can be obtained for designing and optimizing mesh functionalities as well as analyzing the physics and effects of modifying mesh parameters. In the following section, the capability of the *S*-matrix methodology is demonstrated by comparing the performance of the derived closed-form expressions against the results obtained through FDTD for 2×1 and 2×2 mesh devices, which are the fundamental building blocks for creating larger MIM mesh structures.

A. Closed-Form Expression for a 2×1 MIM Mesh

A 2×1 MIM mesh structure consists of two cascaded *X*-junctions, as shown in Fig. 6. Since a portion of the plasmonic wave is reflected every time it reaches a junction, each pair of *X*-junctions will create a localized resonance effect [16]. This weak resonance is controlled by the relative power distribution at each junction and the phase accumulated as the plasmonic wave propagates between junctions. To model the 2×1 mesh, the electric field entering and exiting the structure can be described by a 2×2 *S*-matrix:

$$\begin{bmatrix} Y_1 \\ Y_2 \end{bmatrix} = \begin{bmatrix} S_{11} & S_{12} \\ S_{21} & S_{22} \end{bmatrix} \begin{bmatrix} X_1 \\ X_2 \end{bmatrix}, \tag{4}$$

where

$$S_{11} = r_{J1} + \frac{(t_{J1,2} r_{J2} t_{J1,2} \exp(-\phi))}{1 - r_{J1} r_{J2} \exp(-2\phi)},$$

$$S_{12} = S_{21} = \frac{t_{J1,2} t_{J2,2} \exp(-\phi)}{1 - r_{J1} r_{J2} \exp(-2\phi)},$$

$$\text{and} \quad S_{22} = r_{J2} + \frac{t_{J2,2} r_{J1} t_{J2,2} \exp(-\phi)}{1 - r_{J1} r_{J2} \exp(-2\phi)}.$$

The coefficients r_{J1} and $t_{J1,2}$ denote the reflection and transmission coefficients for the first *X*-junction, and r_{J2} and $t_{J2,2}$ are for the second *X*-junction, all of which are calculated using the modified characteristic impedance model. The phase accumulated between two *X*-junctions is described by $\phi = (\alpha + j\beta)L$, which is dependent on the propagation constant and length of the MIM junction interconnect. The electromagnetic wave exiting this MIM junction resonator can be treated as the summation of an infinite series described as

$$\begin{aligned} E_{\text{out}} &= [\exp(-\phi) + r_{J1} r_{J2} \exp(-3\phi) + r_{J1}^2 r_{J2}^2 \exp(-5\phi) + r_{J1}^4 r_{J2}^4 \exp(-7\phi) + \ldots] E_{\text{in}} \\ &= \frac{\exp(-\phi)}{1 - r_{J1} r_{J2} \exp(-2\phi)} E_{\text{in}}. \end{aligned} \tag{5}$$

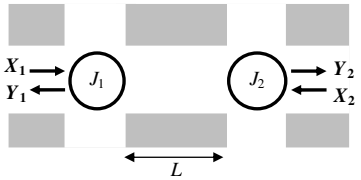

Fig. 6. Schematic and *S*-matrix setup 2×1 MIM mesh structure.

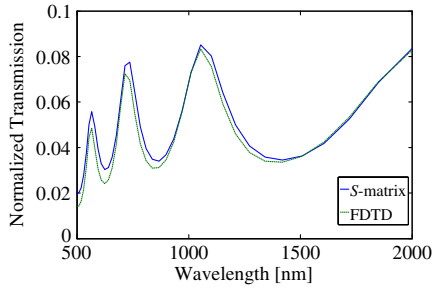

Fig. 7. (Color online) Comparison between the *S*-matrix model and FDTD simulation results of a 2×1 MIM resonator. The structure consists of MIM waveguides with 50 nm cores and a 750 nm long interconnect.

Therefore, all the *S*-matrix elements have a common multiplier $\exp(-\phi)/1 - r_{J1} r_{J2} \exp(-2\phi)$ to account for the infinite reflections within the structure. Assuming single input and identical *X*-junctions, the transmission expression of a 2×1 mesh structure is derived and simplified to be

$$T = \frac{Y_2}{X_1} = \frac{t_2^2 \exp(-\phi)}{1 - r^2 \exp(-2\phi)}. \tag{6}$$

A 2×1 MIM mesh with a 50 nm air core and 750 nm waveguide interconnect is simulated in FDTD and the transmission spectrum closely resembles that of the *S*-matrix model shown in Fig. 7. In addition, localized resonance inside the *X*-junction pair is observed and can potentially be utilized to create feedback and interference effects within a larger MIM mesh structure. Since the *S*-matrix method is only a mathematical framework that relates *X*-junctions represented by the impedance model, it does not provide correction or introduce additional error into the overall performance of the analytical model. Therefore, similar to the case of a single *X*-junction, the analytical prediction deviates from numerical results at lower wavelengths due to the breakdown of equal four-way splitting behavior.

B. Closed-Form Expression for a 2×2 MIM Mesh

The *S*-matrix methodology is next applied to a generic 2×2 MIM mesh structure consisted of four *X*-junctions with eight output ports (Fig. 8). Each pair of *X*-junctions serves as a resonant cavity with feedback into adjacent cavities, creating interference effects at the output. The junction geometry and mesh topology determine the amount of power coupling out of the structure as well as the phase of the plasmonic waves arriving at each junction, thereby influencing the resulting interference patterns and the sustainability of resonance inside

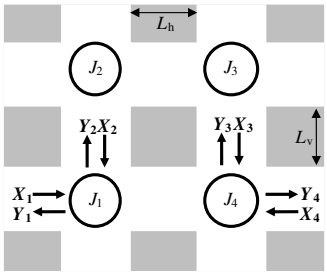

Fig. 8. Schematic and S-matrix setup of a 2×2 MIM mesh structure.

the structure [16]. To model a 2×2 plasmonic mesh, a 4×4 S-matrix can be constructed to obtain the system response:

$$\begin{bmatrix} Y_1 \\ Y_2 \\ Y_3 \\ Y_4 \end{bmatrix} = \begin{bmatrix} S_{11} & S_{12} & S_{13} & S_{14} \\ S_{21} & S_{22} & S_{23} & S_{24} \\ S_{31} & S_{32} & S_{33} & S_{34} \\ S_{41} & S_{42} & S_{43} & S_{44} \end{bmatrix} \begin{bmatrix} X_1 \\ X_2 \\ X_3 \\ X_4 \end{bmatrix}, \tag{7}$$

where

$$S_{11} = r_{J1} + \frac{r_{J4} t_{J1,2}^2 \exp(-2\phi_h)}{1 - r_{J1} r_{J4} \exp(-2\phi_h)},$$

$$S_{12} = j t_{J1,3} + \frac{-j r_{J4} t_{J1,1} t_{J1,2} \exp(-2\phi_h)}{1 - r_{J1} r_{J4} \exp(-2\phi_h)},$$

$$S_{13} = \frac{j t_{J1,2} t_{J4,3} \exp(-\phi_h)}{1 - r_{J1} r_{J4} \exp(-2\phi_h)},$$

$$S_{14} = \frac{t_{J1,2} t_{J4,2} \exp(-\phi_h)}{1 - r_{J1} r_{J4} \exp(-2\phi_h)},$$

$$S_{21} = -j t_{J1,1} + \frac{j r_{J4} t_{J1,2} t_{J1,3} \exp(-2\phi_h)}{1 - r_{J1} r_{J4} \exp(-2\phi_h)},$$

$$S_{22} = r_1 + \frac{r_{J4} t_{J1,1} t_{J1,3} \exp(-2\phi_h)}{1 - r_{J1} r_{J4} \exp(-2\phi_h)},$$

$$S_{23} = \frac{-t_{J1,3} t_{J4,3} \exp(-\phi_h)}{1 - r_{J1} r_{J4} \exp(-2\phi_h)},$$

$$S_{24} = \frac{j t_{J1,3} t_{J4,2} \exp(-\phi_h)}{1 - r_{J1} r_{J4} \exp(-2\phi_h)},$$

$$S_{31} = \frac{-j t_{J1,2} t_{J4,1} \exp(-\phi_h)}{1 - r_{J1} r_{J4} \exp(-2\phi_h)},$$

$$S_{32} = \frac{-t_{J1,1} t_{J4,1} \exp(-\phi_h)}{1 - r_{J1} r_{J4} \exp(-2\phi_h)},$$

$$S_{33} = r_{J4} + \frac{r_{J1} t_{J4,1} t_{J4,3} \exp(-2\phi_h)}{1 - r_{J1} r_{J4} \exp(-2\phi_h)},$$

$$S_{34} = j t_{J4,3} + \frac{-j r_{J1} t_{J4,1} t_{J4,2} \exp(-2\phi_h)}{1 - r_{J1} r_{J4} \exp(-2\phi_h)},$$

$$S_{41} = \frac{t_{J1,2} t_{J4,2} \exp(-\phi_h)}{1 - r_{J1} r_{J4} \exp(-2\phi_h)},$$

$$S_{42} = \frac{-j t_{J1,1} t_{J4,2} \exp(-\phi_h)}{1 - r_{J1} r_{J4} \exp(-2\phi_h)},$$

$$S_{43} = -j t_{J4,1} + \frac{j r_{J1} t_{J4,2} t_{J4,3} \exp(-2\phi_h)}{1 - r_{J1} r_{J4} \exp(-2\phi_h)},$$

$$S_{44} = r_4 + \frac{r_{J1} t_{J4,2}^2 \exp(-2\phi_h)}{1 - r_{J1} r_{J4} \exp(-2\phi_h)}.$$

The factors ϕ_h and ϕ_v represent the phase accumulated in the horizontal and vertical junction interconnects respectively. Since an MIM waveguide only supports TM mode, when the plasmonic wave propagates to a junction, the major field component E_y in the horizontal arms will couple into the major field component E_x of the vertical arms and vice versa. Thus, complex number j is multiplied to the transmission coefficients t_2 and t_3 for all the junctions to account for this cross coupling of electric field components. Furthermore, all of the transmission coefficients t_2 are denoted with a negative sign to account for the asymmetric π phase shift in the X-junction.

In order to solve the closed-form expression for this S-matrix, constitutive relationships are defined between X_2, Y_2, X_3, and Y_3:

$$X_2 = x_1 Y_2 + y_1 Y_3, \qquad X_3 = x_2 Y_3 + y_2 Y_2, \tag{8}$$

where

$$x_1 = r_{J2} \exp(-2\phi_v) + \frac{t_{J2,3} r_{J3} t_{J2,1} \exp(-2\phi_v - 2\phi_h)}{1 - r_{J2} r_{J3} \exp(-2\phi_h)},$$

$$x_2 = r_{J3} \exp(-2\phi_v) + \frac{t_{J3,1} r_{J2} t_{J3,3} \exp(-2\phi_v - 2\phi_h)}{1 - r_{J2} r_{J3} \exp(-2\phi_h)},$$

$$y_1 = -\frac{t_{J3,1} t_{J2,1} \exp(-2\phi_v - \phi_h)}{1 - r_{J2} r_{J3} \exp(-2\phi_h)}, \text{ and}$$

$$y_2 = -\frac{t_{J2,3} t_{J3,3} \exp(-2\phi_v - \phi_h)}{1 - r_{J2} r_{J3} \exp(-2\phi_h)}.$$

Based on the S-matrix and the constitutive relationships, the transmission expression is determined to be

$$\begin{aligned} T = \frac{Y_4}{X_1} &= S_{41} + \frac{S_{21}(S_{42}x_1 + S_{43}y_2)}{1 - S_{22}x_1 - S_{23}y_2} \\ &\quad + \left[S_{42}y_1 + S_{43}x_2 + \frac{(S_{42}x_1 + S_{43}y_2)(S_{22}y_1 + S_{23}x_2)}{1 - S_{22}x_1 - S_{23}y_2} \right] \\ &\quad \times \left[\frac{S_{31} + \frac{S_{21}(S_{32}x_1 + S_{33}y_2)}{1 - S_{22}x_1 - S_{23}y_2}}{1 - S_{32}y_1 - S_{33}x_2 - \frac{(S_{32}x_1 + S_{33}y_2)(S_{22}y_1 + S_{23}x_2)}{1 - S_{22}x_1 - S_{23}y_2}} \right]. \end{aligned} \tag{9}$$

This closed-form expression is verified with a homogeneous plasmonic 2×2 mesh structure where the core width is 50 nm and $L_h = L_v = 750$ nm (Fig. 9). The analytical prediction and FDTD simulation matches well, with a discrepancy of less than 1% despite the breakdown of quasistatic approximation at lower wavelengths. Compared to that of the X-junction

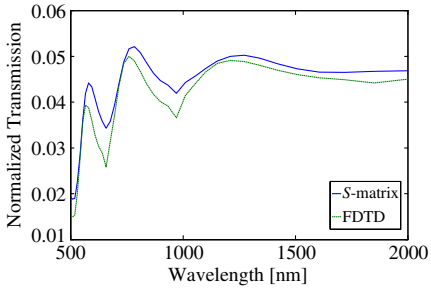

Fig. 9. (Color online) Comparison between the S-matrix model and FDTD simulation results of a 2×2 MIM resonator network. The structure consists of MIM waveguides with 50 nm cores and a 750 nm long interconnect.

pair, the transmission spectrum of this network also displays multiple resonance peaks, but at different wavelengths. Therefore, the interference effect within the mesh network has significantly altered the dispersion characteristics of the structure, and this is useful for engineering the functionality of the overall device.

Because of the symmetry of the structure, by modifying the *S*-matrix elements, Eq. (9) can also be used to obtain the transmission spectrum for output ports connected to the *X*-junctions J_2 and J_4. The closed-form expressions for the remaining output ports can be derived by following the same procedure, but with modifications to the constitutive relations in addition to the *S*-matrix elements. The modelling of multiple-input and multiple-output responses can also be achieved by superimposing transmission spectra generated by the closed-form expressions for excitations from various input ports.

Since the *S*-matrix method used to derive the closed-form expressions is an exact mathematical formulation, any discrepancy between numerical and theoretical results is only attributed to the breakdown of the characteristic impedance model. The error of the impedance model is amplified when the junctions are cascaded to form larger network structures. This increase in mismatch is evident when comparing the discrepancies between analytical and simulation results for a single *X*-junction (Fig. 3), a 2×1 network (Fig. 7), and then a 2×2 structure (Fig. 9).

When defining characteristic impedance for MIM waveguides, the implicit assumption is that these waveguides behave the same way as PEC parallel-plate waveguides. Although these two waveguide configurations are very similar in both structure and modal characteristics, there are still differences, such as their relative strength between transverse field components and their modal penetration into the metallic claddings. Moreover, there are additional loss mechanisms in MIM junctions that are not accounted for by the impedance model, since they do not take place for PEC parallel-plate waveguides. For example, higher-order MIM modes can be induced at the center of the junction, and electromagnetic waves can be scattered at the corner of the junction. These loss mechanisms are evident in Figs. 7 and 9, where the shape of the spectral responses generated numerically is almost identical to the ones generated analytically, but with slightly lower amplitude. Since optical power does not always split equally among symmetric junction arms, an MIM *X*-junction cannot always be treated as four transmission lines connected in series. Thus, even exact methods such as *S*-matrix and impedance models should only be treated as approximations that are highly accurate. In both2×2 and 2×1 mesh structures, however, the discrepancies are only a few percent or less across a large spectrum. Thus, the proposed closed-form model is already a powerful and adequate tool for accurate and efficient analysis of MIM mesh architectures. In other words, we now have the framework for the design and optimization of generalized MIM junction-based devices without relying on numerically extracted parameters.

4. MIM MESH ATTRIBUTES AND *S*-MATRIX MODEL VERSATILITY

The topology of an MIM mesh structure can be engineered in many ways to match the output transmission response to a desired function. By terminating some of the output ports within a network of interconnected MIM junctions, various stub structures can be created. By introducing width differences between the network output ports and the internal junction interconnects, the localized resonance in the network can be fine-tuned for wavelength-selective applications. This resonance effect can be even further enhanced by designing width discontinuities along the interconnects. The generalized *S*-matrix impedance model can accommodate these different design freedoms with a minimal increase in the required computational cost.

A. Stub-Loaded Filter Using a 2×1 MIM Mesh

MIM stub structures have been proposed for various sensing and demultiplexing applications [20,24]. By treating stubs as junctions with terminating arms, our S-matrix design model is also applicable to generic MIM stub structures.

To demonstrate our model's capability for designing stub-loaded devices, a 2×1 MIM mesh consisted of two double-sided stubs [Fig. 10(b)] is analyzed for a band-reject filter application. The structure is similar to the cascaded *X*-junction pair displayed in Fig. 6, but with all the vertical ports terminated. Therefore, the analytical expression for the power distribution in an *X*-junction with terminating vertical ports [Fig. 10(a)] needs to be derived first, and then Eq. (6) can be applied to obtain the transmission spectrum of the overall stub structure.

The powers entering and exiting the arms of a single input and single output (X′1 = 1 and X′4 = 0) closed *X*-junction are described by the following 4×4 *S*-matrix and constitutive relationships:

$$\begin{bmatrix} Y_1' \\ Y_2' \\ Y_3' \\ Y_4' \end{bmatrix} = \begin{bmatrix} S_{11} = r & S_{12} = t_3 & S_{13} = t_1 & S_{14} = 0 \\ S_{21} = t_1 & S_{22} = r & S_{23} = t_2 & S_{24} = 0 \\ S_{31} = t_3 & S_{32} = t_2 & S_{33} = r & S_{34} = 0 \\ S_{41} = t_2 & S_{42} = t_1 & S_{43} = t_3 & S_{44} = 0 \end{bmatrix} \begin{bmatrix} X_1' \\ X_2' \\ X_3' \\ X_4' \end{bmatrix}, \tag{10}$$

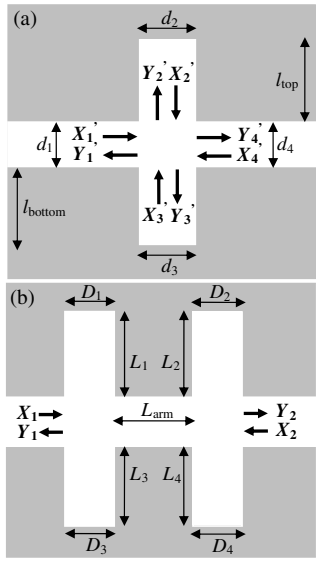

Fig. 10. Schematic and *S*-matrix setup of (a) a MIM *X*-junction with closed vertical ports and (b) a MIM mesh with two double-side stubs.

$$X'_2 = r_{\text{top}} Y'_2, \qquad X'_3 = r_{\text{bottom}} Y'_3, \tag{11}$$

where $r_{\text{top}} = -\exp(2l_{\text{top}}(\alpha_{\text{top stub}} + j\beta_{\text{top stub}}))$ and $r_{\text{bottom}} = -\exp(2l_{\text{bottom}}(\alpha_{\text{bottom stub}} + j\beta_{\text{bottomstub}}))$.

The elements of this S-matrix are the power distribution ratio of a regular X-junction with four open ports, and r_{top} and r_{bottom} represent the phase accumulation as well as the power attenuation acquired as plasmonic wave propagates within the stubs. Both reflection coefficients have a negative sign, since the reflection at the end of the stub results in a π-phase shift.

By solving the S-matrix using the constitutive relationships, the transmission expression of the closed X-junction is derived to be

$$T' = S_{41} + \frac{S_{42}S_{21}r_{\text{top}}}{1 - S_{22}r_{\text{top}}} + r_{\text{bottom}}\left(\frac{S_{42}S_{23}r_{\text{top}}}{1 - S_{22}r_{\text{top}}} + S_{43}\right) \times \left(\frac{S_{31} + \frac{S_{32}S_{21}r_{\text{top}}}{1 - S_{22}r_{\text{top}}}}{1 - r_{\text{bottom}}S_{33} + \frac{S_{32}S_{23}r_{\text{top}}}{1 - S_{22}r_{\text{top}}}}\right). \tag{12}$$

Moreover, the same expression can be used to obtain the reflection coefficient of the closed X-junction by replacing S_{41}, S_{42}, and S_{43} with S_{11}, S_{12}, and S_{13}.

Once the transmission and reflection coefficients for both closed X-junctions are obtained and substituted back into Eq. (6), the closed-form transmission expression can be solved and then plug into MATLAB optimization procedure to create band-reject filter response. In Fig. 11, the comparisons between the transmission and phase spectra obtained from the S-matrix model and FDTD simulation are displayed. The optimized double stubbed MIM structure has parameters $L_1 = L_2 = 325$ nm, $L_3 = L_4 = 100$ nm, $L_{\text{arm}} = 200$ nm, and a core width of 100 nm. Our model demonstrates good agreement with simulation results and the device has a 250 nm wide bandpass response centered at 900 nm and a 300 nm wide band-reject response centered at 1500 nm.

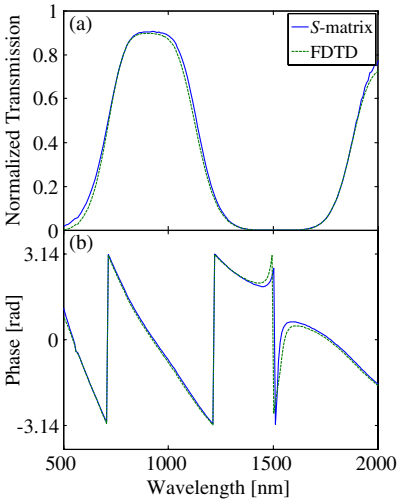

Fig. 11. (Color online) (a) Intensity and (b) phase comparison between FDTD and S-matrix modeling results for a homogeneous double-stubbed MIM structure where $L_1 = L_2 = 325$ nm, $L_3 = L_4 = 100$ nm, and $L_{\text{arm}} = 200$ nm. The structure is optimized for a band-reject response centered at $\lambda = 1550$ nm.

Although the S-matrix model is utilized for the optimization of a 2×1 double-sided MIM stub network, it can be extended to analyze MIM stub-loaded mesh in general. Single-sided stubs can be modeled by setting the S-matrix elements S_{13}, S_{23}, S_{31}, S_{32}, and S_{33} to zero. Moreover, Eq. (6) can be utilized to include additional stubs in the structure. Overall, the model lends itself for efficient design of not only MIM junctions but also MIM stub structures.

B. Resonance in a 2D MIM Mesh

From our closed-form model, some insight can be inferred about how one can utilize the localized resonance within MIM mesh structures for wavelength-selective applications. The resonant wavelength within a network is determined by the length and the width of the interconnects between the various junctions. To enhance the resonance effect within the network, the widths of the interconnects can be made wider than those of the output waveguide ports such that the amount of internal reflection is increased (Fig. 12). The higher reflectivity can be utilized to reinforce the resonance effect while keeping the dimensions of the MIM mesh structures in the nanoscale so that the amount of metal absorption loss can be minimized.

The localized resonance in a 2D MIM mesh is investigated in a network with $L_1 = L_2 = 800$ nm, $d_1 = d_2 = 100$ nm, and $d_3 = d_4 = 150$ nm. The results based on our model and FDTD calculations demonstrate good agreement, as shown in Fig. 13. The output optical powers are distributed at each X-junction, where one output arm exhibits selective transmission at the telecom wavelength whereas the other exhibits the complementary notch filter response. The Q-factor of this 2×2 MIM network is 62, which is slightly lower than the previously reported value of 72 [16]. Nonetheless, our network is only 800 nm in length as opposed to 6 μm in the previous design and thus there is a significant increase in the amount of transmitted output power. The effects of varying the parameters of junction interconnects are shown in Fig. 14. At output port 7, an increase in length shifts the resonance peak toward a higher wavelength, whereas an increase in width shifts the peak toward a lower wavelength. It is also observed that a change in length introduces a larger resonance shift compared to that of a change in width. Thus, using the width of the interconnect to fine-tune the location of the resonance peak can result in enhanced fabrication tolerance for 2D MIM mesh devices.

C. Modified 2D Mesh with Enhanced Characteristics

In addition to using the relative width of the junction arms to minimize the amount of light coupling out of the network

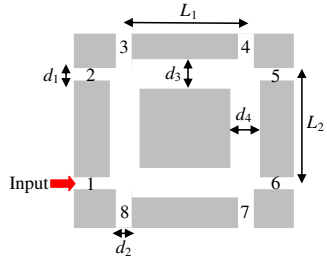

Fig. 12. (Color online) Schematic of a 2D MIM mesh structure with widened internal network waveguides. The structure can be modeled analytically using the S-matrix setup illustrated in Fig. 8.

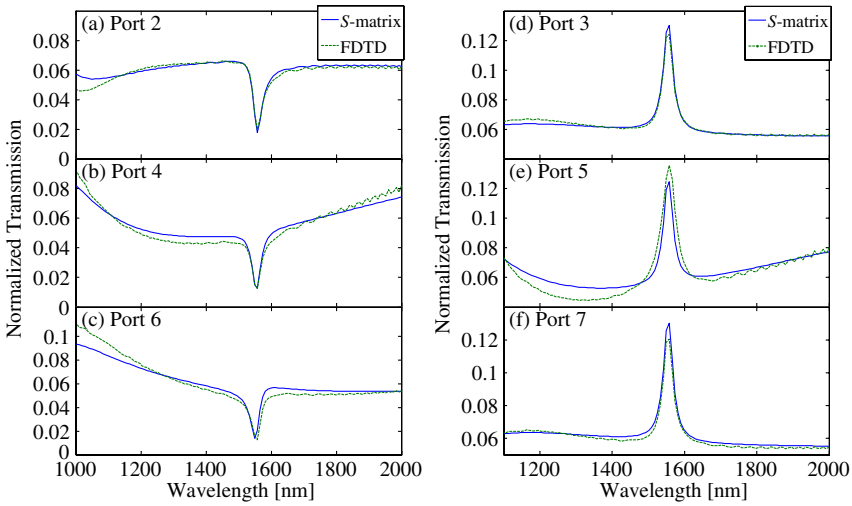

Fig. 13. (Color online) Normalized transmission at different output ports of a 2D MIM mesh with widened internal waveguide interconnects. The network output arms have 100 nm cores, and the internal interconnects are 800 nm long with 150 nm cores.

structure, the resonance effect can be even further enhanced by creating width discontinuities along the interconnects. For sensing and nonlinear applications, the mesh network may need to be filled with polymers or quantum dots at designated locations. The width of the discontinuity relative to the size of nanoparticles can potentially be used as the control parameter for selective filling.

The *S*-matrix model can incorporate the interconnect width discontinuity and thus adds another degree of design freedom to MIM mesh devices. Similar to the homogeneous 2×2 MIM mesh, where the MIM core width is constant, the new structure can be treated as four cascaded X-junctions [Fig. 15(a)]. However, one of the junction arms would include a widened MIM section [Fig. 15(b)]. To determine the power distribution ratio of this modified junction, the widened waveguide section [Fig. 15(c)] can be treated as a Fabry–Perot cavity, and the transmission and reflection coefficients are determined based on the characteristic impedance model to be

$$R = R_1 + \frac{R_3 T_1 T_2 \exp(-2\phi_B)}{1 - R_2 R_3 \exp(-2\phi_B)} \quad \text{and} \quad T = \sqrt{1 - R^2}, \tag{13}$$

where

$$R_1 = \left|\frac{Z_B - Z_A}{Z_B + Z_A}\right|, \qquad R_2 = \left|\frac{Z_A - Z_B}{Z_B + Z_A}\right|, \qquad R_3 = \left|\frac{Z_C - Z_B}{Z_B + Z_C}\right|,$$
$$T_1 = \sqrt{1 - R_1^2}, \qquad T_2 = \sqrt{1 - R_2^2}.$$

The factors Z_A, Z_B, and Z_c are the impedances for MIM waveguide sections A, B, and C, respectively and $\phi_B = (\alpha_B + j\beta_B)L_B$ is the phase accumulated in section B.

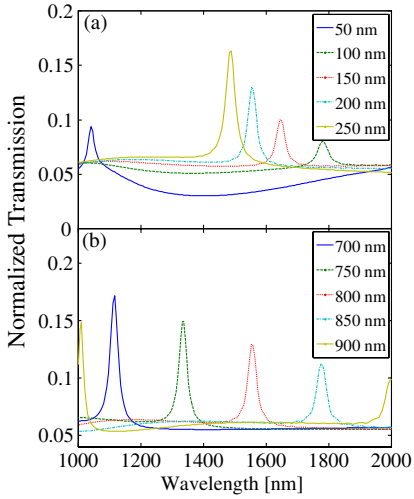

Fig. 14. (Color online) Normalized transmission of output port 7 of a 2D MIM mesh with (a) 150 nm wide network interconnects with varying lengths and (b) 800 nm long network interconnects with varying widths. The widths of the output arms are kept constant at 100 nm.

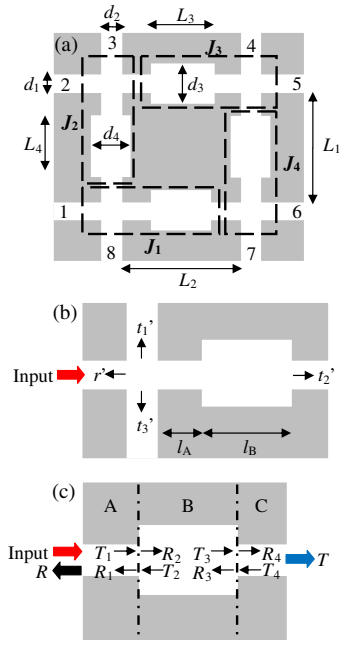

Fig. 15. (Color online) Schematic of a 2×2 MIM mesh with (a) width discontinuity in the interconnects, (b) a modified X-junction that includes width discontinuity, and (c) an interconnect discontinuity.

With excitation from the left horizontal arm, the power distribution ratio for the modified X-junction as shown in Fig. 15(b) can then be redefined as

$$
\begin{aligned}
r' &= r + \frac{t_2^2 R \exp(-2\phi_A)}{1 - Rr}, \\
t_1' &= t_1 + \frac{t_2 R t_3 \exp(-2\phi_A)}{1 - Rr}, \\
t_2' &= t_2 T + \frac{t_2 R r T \exp(-3\phi_A)}{1 - Rr}, \\
t_3' &= t_3 + \frac{t_2 R t_1 \exp(-2\phi_A)}{1 - Rr},
\end{aligned} \tag{14}
$$

where r, t_1, t_2, and t_3 are the power distribution ratio of an X-junction without the cascaded discontinuity section and $\phi_A = (\alpha_A + j\beta_A)L_A$ is the phase accumulated in waveguide section A. Since the junction arms are not identical, four sets of transmission and reflection coefficients associated with the different direction of junction excitation will need to be obtained individually using the same procedure.

The effect of introducing additional cavities is demonstrated in Fig. 16 by the comparison between FDTD-generated transmission spectrum for a regular 2D mesh with constant interconnect width (Design 1) and that of a resonance-enhanced 2D mesh with interconnect width discontinuity (Design 2). The parameters of Design 1 are $d_1 = d_2 = d_3 = d_4 = 40$ nm, $L_1 = L_2 = 820$ nm, and $L_3 = L_4 = 0$ nm, whereas the parameters of Design 2 are $d_1 = d_2 = 40$ nm, $d_3 = d_4 = 100$ nm, $L_1 = L_2 = 960$ nm, and $L_3 = L_4 = 700$ nm. For both networks, output ports 3, 4, 7, and 8 are closed to conserve the optical power in the structure. Although the optimized design is slightly larger, the amount of transmitted power does not degrade and the full-width half-maximum of the localized resonance is reduced by half [Fig. 16(c)]. This enhancement is the result of additional resonant cavities created by the widened interconnect section that has lower propagation loss. It can also be observed that the resonance peaks at outputs 2 and 6 are shifted when the discontinuities are introduced. Therefore, the length of these discontinuities is an additional control parameter for fine-tuning the location of the resonance peaks. Finally, our S-matrix model demonstrates good agreement with FDTD results, with discrepancies of less than 2%. Thus, it is confirmed to be capable of accurately modeling generalized MIM mesh structures with stubs, closed ports, and width discontinuities.

5. DISCUSSION

The combination of the modified impedance model and the S-matrix formulation addresses the need for a purely analytical method for the investigation of junction-based MIM structures. Although the impedance model has previously been incorporated into the S-matrix microwave design methodology for the design of one-dimensional MIM Bragg reflectors [25] and mode converters [21], it has not been extended for 2D network structures. In addition, our model accounts for phase accumulation and the resonance effect inherent in junction pairs such that interference, resonance, and feedback effects can all be accurately and analytically investigated. The feedback effect in an MIM network [18] was previously modeled with a similar mathematical treatment, but the study did not take into account the multiple reflection effect between T-junctions, which is considerably less than the internal reflection between X-junctions. Our model demonstrates higher accuracy by including the contribution of wave reflections, which can be significant for generalized mesh structures.

The significance of formulating closed-form expressions is the ability to analyze MIM mesh structures without the need to perform FDTD simulations and/or create a precompiled parameter space. This leads to significantly shorter computational cycle and smaller memory requirement. The closed-form expressions capture the interrelations of various S-matrix elements and therefore can provide physical insights into the effects of manipulating network topologies. These physical effects are concealed if numerical simulations are performed or the exact solutions of Maxwell's equations are solved. The proposed model is an all-purpose analytical framework that can be adapted to model MIM structures for specific applications. Therefore, the required computational resources for device optimization do not scale dramatically with the complexity or dimension of the MIM structure.

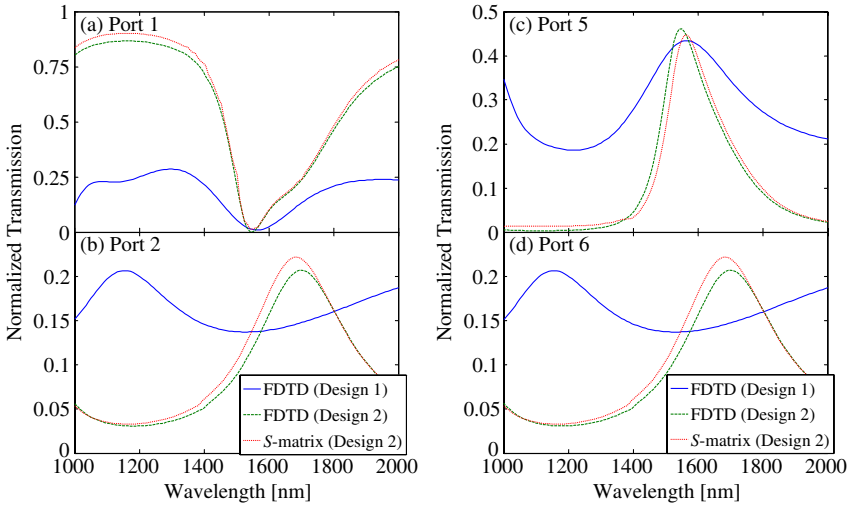

Fig. 16. (Color online) Comparison of transmission spectra between FDTD simulation and the S-matrix model for an enhanced 2×2 mesh with width discontinuity along the interconnect (Design 2) for output ports (a) 1, (b) 2, (c) 5, and (d) 6. The FDTD spectrum for a regular 2×2 mesh without discontinuity is also plotted as a reference (Design 1).

Modifications to the mesh structure only require changes to the S-matrix elements, which are encapsulated in the overall transmission expression that remains unchanged. Thus, an efficient design process is possible by treating the MIM mesh architecture as a black box with a set of input and output parameters. One can envision potentially incorporating such encapsulation into microwave or electronic circuit design software for examining optoelectronic circuits.

In addition to reducing the design cycle duration, the closed-form model can also be utilized for device sensitivity analysis. This can be done by taking the derivative of transmission expressions such as Eqs. (6) and (9) with respect to each parameter. The critical parameters and dominant physical interactions within a multi-variable network device can then be identified analytically.

Another advantage of employing our closed-form model is that individual MIM networks can be replaced with respective analytical expressions and then easily integrated to analyze larger and more complex network configurations. The 2×1 and 2×2 networks can be treated as the building blocks for mesh architectures in general, since larger structures can be broken down into a combination of either component. Thus, Eq. (6), which describes the interaction of two cascaded X-junctions, can be applied to larger networks by replacing the transmission response of individual X-junctions with that of 2×1 and/or 2×2 networks. Equations (10–14) then allow the manipulation of topological parameters to create more complex mesh configurations. However, despite the scalability of our model, the significant metal absorption loss prohibits the device footprint from expanding into the microscale. The rich resonance and feedback effects between X-junction pairs effectively increase the overall distance that the plasmonic waves propagate. This in turn limits the amount of transmitted output power as shown in Figs. 9, 13, and 16. Thus, extending the mesh structures beyond their current 2×2 configurations may not be practical.

Although our investigation focuses on 2D network devices that are truncated in the vertical dimension, the closed-form model remains effective for realistic network structures that extend into the third dimension. Similar to its 2D counterpart, a subwavelength 3D MIM waveguide supports quasi-TEM modes with electric field predominantly in the direction parallel to the waveguide core. However, the mode profile now includes edge effects that disrupt the uniformity and the confinement of the electromagnetic field. Therefore, the exact formulation of waveguide characteristic impedance is required. In this case, the effective voltage and current need to be calculated by a direct integral of field components along the waveguide's cross section [26]. Nonetheless, the S-matrix formulation would remain the same, and therefore the transmission expressions derived for the various mesh structures in this study remain valid for 3D MIM waveguide configuration.

Introducing the third dimension, however, creates additional modeling constraints due to additional loss mechanisms such as the excitation of 2D plasmon modes, out-of-plane radiation, and local heating that occurs at the edge of the junction [26]. This means that the performance of functional devices fabricated in reality will deteriorate slightly compared to their 2D counterparts. Figure 17 shows the breakdown of equal four-way splitting behavior in a 3D symmetric

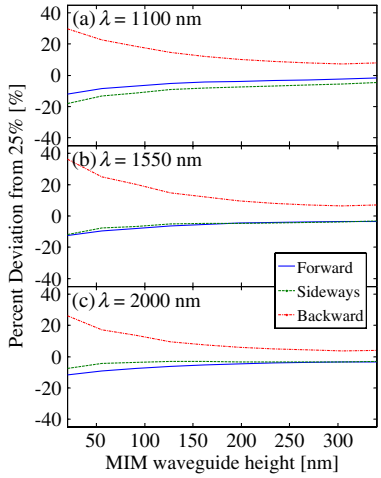

Fig. 17. (Color online) Model limitation demonstrated by the percent deviation from equal power splitting (25%) in a symmetric 50 nm X-junction at (a) $\lambda = 1100$ nm, (b) $\lambda = 1550$ nm, and (c) $\lambda = 2000$ nm. The data are extracted from 3D FDTD simulations.

X-junction at different wavelengths. The core width of the junction is kept at 50 nm, while the height of the junction is varied. It can be observed that the edge effects induce significant reflection, particularly at lower wavelengths and for waveguides with low aspect ratios. However, as the wavelength and/or the height of the waveguide are increased, the waveguide modal profile starts to resemble that of its 2D counterpart and the edge effects are suppressed. When the junction is taller than 200 nm, the power distribution at a 3D symmetric X-junction only deviates from equal splitting by less than 5%. Therefore, the impedance model in combination with the S-matrix method remains a reliable tool, even for analyzing generalized 3D MIM mesh structures with high aspect ratios. One method to extend the model's region of validity for 3D structures is to introduce a bending curvature to the corners of the junctions to alleviate the amount of scattering loss at the edges [26]. The established techniques for the fabrication of MIM mesh structures are focused ion beam [7] and electron beam lithography [27], both of which will intrinsically create junctions with rounded edge corners.

6. CONCLUSION

A generic analytical model for 2D MIM mesh structures is presented by incorporating the characteristic impedance model for MIM junctions into the S-matrix formalism. We modified the impedance model to include waveguide loss and phase accumulation and demonstrated for the first time that it can provide a full description of the behavior of generalized X-junctions. It was determined that when the width of the waveguide core is close to 120 nm, the dielectric discontinuity at the center of the junction does not induce attenuation or phase changes. This enables an S-matrix representation of MIM networks that takes into account the interference, resonance, and feedback effects within the structure. Closed-form expressions were derived for 2×1 and 2×2 mesh structures, thereby eliminating the need for computationally intensive simulations or precompiled parameter space while showing good agreement with numerical results. Since the 2×1 and 2×2 networks are the building blocks for MIM network structures, the existing model can be extended to accommodate

more complex mesh structures and offers the ability to handle arbitrary combinations of junctions. Therefore, our model serves as an all-purpose analytical framework that is scalable and can be adapted to model specific MIM structures and perform device sensitivity analysis. We also suggested potential device design techniques such as closing output ports, designing width differences between junction arms, and engineering width discontinuity along the junction interconnect. Although we focused on 2D MIM mesh structures in this work, the same design methodology can be applied to larger, nonorthogonal, or even 3D configurations of MIM mesh structures.

REFERENCES

1. J. Homola, "Present and future of surface plasmon resonance biosensors," Anal. Bioanal. Chem. **377**, 528–539 (2003).
2. S. A. Maier, "Plasmonic field enhancement and SERS in the effective mode volume picture," Opt. Express **14**, 1957–1964 (2006).
3. E. Ozbay, "Plasmonics: merging photonics and electronics at nanoscale dimensions," Science **311**, 189–193 (2006).
4. J. A. Dionne, L. A. Sweatlock, and H. A. Atwater, "Plasmonic slot waveguides: towards chip-scale propagation with subwavelength-scale localization," Phys. Rev. B **73**, 035407 (2006).
5. L. Chen, J. Shakya, and M. Lipson, "Subwavelength confinement in an integrated metal slot waveguide on silicon," Opt. Lett. **31**, 2133–2135 (2006).
6. P. Berini, "Bulk and surface sensitivity of surface plasmon waveguides," New J. Phys. **10**, 105010 (2008).
7. B. Lau, M. A. Swillam, and A. S. Helmy, "Hybrid orthogonal junctions: wideband plasmonic slot-silicon waveguide couplers," Opt. Express **18**, 27048–27059 (2010).
8. R. Zia, J. A. Schuller, A. Chandran, and M. L. Brongersma, "Plasmonics: the next chip-scale technology," Mater. Today **9**, 20–27 (2006).
9. Y. Guo, L. Yan, W. Pan, B. Luo, K. Wen, Z. Guo, H. Li, and X. Luo, "A plasmonic splitter based on slot cavities," Opt. Express **19**, 13831–13838 (2011).
10. Z. Han, L. Liu, and E. Forsberg, "Ultra-compact directional couplers and Mach-Zehnder interferometers employing surface plasmon polaritons," Opt. Commun. **259**, 690–695 (2006).
11. C. Min and G. Veronis, "Absorption switches in metal-dielectric-metal plasmonic waveguides," Opt. Express **17**, 10757–10766 (2009).
12. F. Hu, H. Yi, and Z. Zhou, "Wavelength demultiplexing structure based on arrayed plasmonic slot cavities," Opt. Lett. **36**, 1500–1502 (2011).
13. G. Veronis and S. Fan, "Bends and splitters in metal-dielectric-metal subwavelength plasmonic waveguides," Appl. Phys. Lett. **87**, 131102 (2005).
14. E. Feigenbaum and M. Orenstein, "Perfect 4-way splitting in nano plasmonic *X*-junctions," Opt. Express **15**, 17948–17953 (2007).
15. F. Hu and Z. Zhou, "Wavelength filtering and demultiplexing structure based on aperture-coupled plasmonic slot cavities," J. Opt. Soc. Am. B **28**, 2518–2523 (2005).
16. E. Feigenbaum and H. Atwater, "Resonant guided wave networks," Phys. Rev. Lett. **104**, 147402 (2010).
17. M. A. Swillam and A. S. Helmy, "Filter response of feedback plasmonic junctions," in *Integrated Photonics Research, Silicon and Nanophotonics*, OSA Technical Digest (CD) (Optical Society of America, 2011), paper ITuD4.
18. M. A. Swillam and A. S. Helmy, "Feedback effects in plasmonic slot waveguides examined using a closed-form model," Photon. Technol. Lett. **24**, 497–499 (2012).
19. H. Nejati and A. Beirami, "Theoretical analysis of the characteristic impedance in metal-insulator-metal plasmonic transmission lines," Opt. Lett. **37**, 1050–1052 (2012).
20. A. Pannipitiya, I. D. Rukhlenko, M. Premaratne, H. T. Hattori, and G. P. Agrawal, "Improved transmission model for metal-dielectric-metal plasmonic waveguides with stub structure," Opt. Express **18**, 6191–6204 (2010).
21. S. E. Kocabas, G. Veronis, D. A. B. Miller, and S. Fan, "Modal analysis and coupling in metal-insulator-metal waveguides," Phys. Rev. B **79**, 035120 (2009).
22. Lumerical, "Multicoefficient material modelling in FDTD," http://www.lumerical.com/solutions/whitepapers/fdtd_multicoefficient_material_modeling.html.
23. D. Dai and S. He, "A silicon-based hybrid plasmonic waveguide with a metal cap for nano-scale light confinement," Opt. Express **17**, 16646–16653 (2009).
24. X. Lin and X. Huang, "Tooth-shaped plasmonic waveguide filters with nanometeric sizes," Opt. Lett. **33**, 2874–2876 (2008).
25. A. Hosseini, H. Nejati, and Y. Massoud, "Modeling and design methodology for metal-insulator-metal plasmonic Bragg reflectors," Opt. Express **16**, 1475–1480 (2008).
26. W. Cai, W. Shin, S. Fan, and M. L. Brongersma, "Elements for plasmonic nanocircuits with three-dimensional slot waveguides," Adv. Mater. **22**, 5120–5124 (2010).
27. J. Tian, S. Yu, and M. Qiu, "Broadband high-efficiency surface-plasmon-polariton coupler with silicon-metal interface," Appl. Phys. Lett. **95**, 013504 (2009).